PERFORMANCE CHARACTERIZATION OF PROCESS MONITORING SENSORS ON THE NIST ADDITIVE MANUFACTURING METROLOGY TESTBED

B. Lane[1], S. Grantham[2], H. Yeung[1], C. Zarobila[2], J. Fox[1]

[1]Engineering Laboratory, [2]Physical Measurement Laboratory,
National Institute of Standards and Technology, Gaithersburg, MD 20899

Abstract

Researchers and equipment manufacturers are developing in-situ process monitoring techniques with the goal of qualifying additive manufacturing (AM) parts during a build, thereby accelerating the certification process. Co-axial melt pool monitoring (MPM) is one of the primary in-situ process monitoring methods implemented on laser powder bed fusion (LPBF) machines. A co-axial MPM system is incorporated on the Additive Manufacturing Metrology Testbed (AMMT) at the National Institute of Standards and Technology (NIST); a custom LPBF and thermophysical property research platform where one of many research goals is to advance measurement science of AM process monitoring. This paper presents the methods used to calibrate and characterize the spatial resolution of the melt pool monitoring instrumentation on the AMMT. Results from the measurements are compared to real melt pool images, and analysis is provided comparing the effect on spatial resolution limits on image analysis.

Introduction

Process monitoring for additive manufacturing describes a suite of sensor technologies that may be applied in-situ during an additive manufacturing (AM) build, with the goal of providing a record of the build by correlating the sensor signals with various part qualities or defects. This quality record may then be used as substitute for costly and time-intensive ex-situ part or material qualification. This concept is described with multiple names; e.g., *rapid qualification* [1], *certify-as-you-build* [2], and *in-process quality assurance* [3], and the types of sensor systems and applications used are widely reviewed [4–8]. For laser powder bed fusion (LPBF) process, one of the most promising technologies is co-axial melt pool monitoring (MPM), which is already appearing on commercial LPBF systems.

Co-axial MPM uses an imaging detector (camera) and/or photodetectors aligned co-axially along the optical path of the laser using a beam splitter, such that optical emission from the melt pool are captured stationary within the field of view of the sensors while the laser scans over the powder layer. These signals or images are then processed and parameterized. For example, length, width, area, or intensity may be calculated from melt pool images [9], then mapped to the spatial coordinates within the volume of a part, and correlated to part quality or defects measured ex-situ. Additionally, these in-situ coordinates may be correlated to X-ray computed tomography (XCT) measurements of part porosity [10,11]. Of course, the resolution of this spatial mapping is set by the temporal resolution of the co-axial sensors combined with the scanning speed of the co-located laser spot and imager field of view. Several works have looked at the temporal resolution or sampling rate requirements for MPM systems [10,12,13].

Similarly, there are spatial resolution requirements for evaluation of melt pool images themselves as opposed to the resolution for spatially mapping the melt pool data within the 3D part space. Most AM process monitoring literature using imaging techniques provides only a statement of the measurement system's instantaneous field of view (iFoV), which is the equivalent size of the detector pixel projected onto the object plane (μm per pixel). The ratio of the iFoV to the detector pixel size is equal to the

magnification of the system. The pixel pitch is the distance between centers of adjacent pixels on the detector. Grasso et al. provide a good review of the various iFoV sizes for multiple co-axial (image coordinates move with the laser) and staring (image coordinates are fixed) AM process monitoring systems [5]. However, the iFoV is not the technically correct definition of image resolution, which can be limited by inherent blurring from the optical system. This blurring, and the contributing image degradation stemming from components within the measurement system, can be described by modulation transfer functions (MTFs), which are further described later in this paper. Lott et al. provided one of the few examples of characterization of the optical system performance of a co-axial MPM system [14].

This spatial resolution is ultimately set by 1) the performance of the optics, 2) characteristics of the imaging detector, and 3) the image processing algorithms used to parameterize the melt pool image. The scope of this paper primarily deals with the first two, while providing an example of the third applied to co-axial melt pool images. Measured spatial resolution of the co-axial MPM system is measured and compared against the modeled optimal performance. The goals of this paper are to 1) evaluate performance of the melt pool monitoring system, primarily regarding image resolution, and 2) give example measurements and examine the effect of limiting resolution on melt pool image analysis. Ultimately, for co-axial MPM and process monitoring to be useful in rapid qualification, standard characterization of the system performance, including spatial resolution, is necessary, as is the understanding of its effect on melt pool image processing.

Co-axial Melt Pool Monitoring System Spatial Resolution

Description of the laser injection and process monitoring optical paths on the AMMT, including system modeling and design, was provided in [15]. The system was designed using Zemax[1] modeling software to enable 1x magnification imaging of the melt pool optimized at 850 nm ± 25 nm waveband, while being constrained to enable a 100 μm full-width half max (FWHM) focused laser spot at 1070 nm wavelength. To avoid chromatic aberrations inherent with an f-theta lens, it utilizes a linear translating z-lens (LTZ) to maintain a planar focus of the laser and imager.

Two imagers are tested in this paper; a high speed, low resolution camera (pixel pitch = 20 μm), and a low speed, high resolution camera (pixel pitch = 1.67 μm). Given the 1:1 magnification design, the iFoV is equal to each detector's pixel pitch (measured to be within 1%). The high speed camera, capable of frame rates in excess of 100 000 frames per second, is utilized to research high speed melt pool dynamics [13]. The low speed camera is a general purpose, gigabit Ethernet (GigE) camera, not suitable for the high temporal bandwidth requirements for MPM. The fine detector pitch of the GigE camera can be used to measure the optical performance of the system, without being limited by detector size.

Knife-Edge Measurement of Modulation Transfer function (MTF)

The modulation transfer function (MTF) provides a more comprehensive definition of spatial resolution for an imaging system. For a measured object with spatially modulated intensity, the MTF is the ratio of the optical system output over the modulated intensity input, at a specific spatial frequency [16,17]. It is essentially the Fourier transform of the impulse response (point spread function, PSF), or a measure of the 'blurriness' of an image, but in frequency space. When the MTF = 0, this means the relative intensities of adjacent bright and dark parts of a measured object are the same, resulting in zero difference or contrast

---

in intensity in the corresponding image. A commonly cited definition of 'spatial resolution' is given as the 10 % of the MTF curve [17], or the spatial frequency at which the contrast is 90 % attenuated.

An optical system MTF can be considered to be composed of multiple components that describe the system, such as the optics (MTF_{optics}), the detector ($MTF_{detector}$), or even aberrations, defocusing, motion blur, etc [17]. By comparing the modeled system MTFs vs. measured, much can be learned about the real system performance vs. optimal design. For the co-axial MPM system analyzed here, we consider the system composed of the optics and the detector:

$$MTF_{system} = MTF_{detector} \cdot MTF_{optics}. \tag{1}$$

The MTF of the AMMT co-axial MPM system was determined from Zemax optical modeling software during the system design [15]. The design enables diffraction limited performance, which provides the maximum throughput (or minimum attenuation) physically limited by the wavelength and optics geometry. $MTF_{optics}(f) = 0$ when $f_0 = 1/\lambda N$, where N is the f-number of the system, λ is the light wavelength, and f is the spatial frequency (cycles/mm).

MTFs for a detector with square pixels can be computed as $MTF_{detector}(f) = |\text{sinc}(w \cdot f)|$, where w is the pixel pitch (mm/pixel). This means the 0% cutoff ($MTF_{detector}(f) = 0$) occurs at $f_0 = 1/w$. It should be noted that this calculation assumes square pixels, and provides the MTF along the primary detector axes, whereas the MTF along diagonals or for non-square detectors are more complicated [16]. However, the simpler approximation suffices for the analysis made in this paper.

The MTF_{system} can be measured by performing a knife edge (KE) measurement, as shown in Figure 1 for the co-axial MPM system and two detector types. A KE measurement is made by imaging a well-focused straight edge that splits uniform light and dark portions of an image. In Figure 1, this was accomplished by setting a razor blade on top of a fiber illuminator. The co-axial MPM imager was focused on the KE, while the fiber end was at a defocused distance below the KE, and covered with Teflon tape to act as a diffuser.
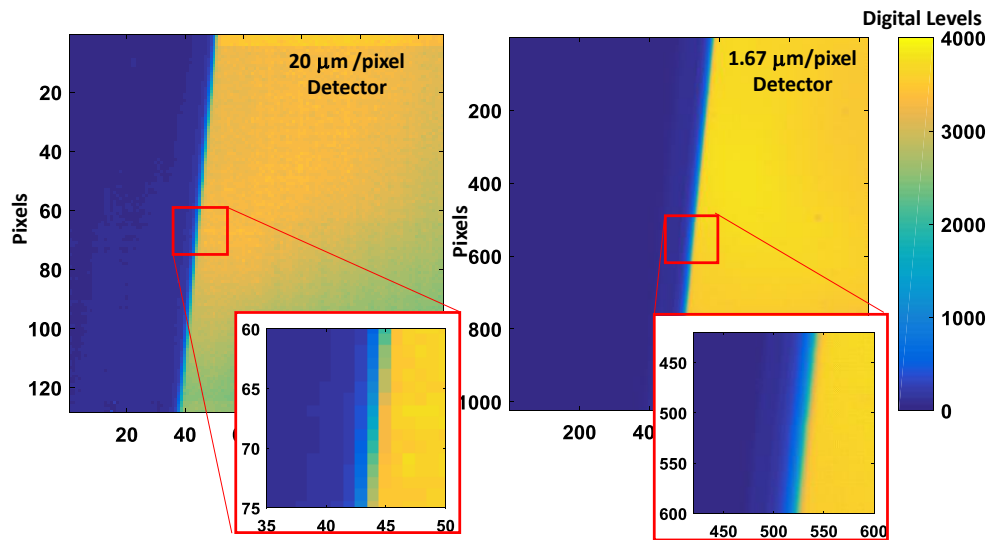

Figure 1: Knife-edge image results for both detectors, showing the finer detail in the 1.67 μm detector measurement. Image axes are in pixels, and are scaled to approximately the same geometric dimensions.

To compute the measured MTFs from the KE images, a custom code was written that performs the methodology defined in ISO 12333 [18,19]. In short, multiple line profiles orthogonal to the KE (x vs. digital level) are sampled, resulting in an edge spread function (ESF). The MTF is then computed as the Fourier transform of the spatial derivative (d/dx) of the ESF. Further description of this algorithm is given in [20]. Figure 2 provides the results of the measured MTF_{system} utilizing the 20 μm and 1.67 μm detectors, and comparison to the MTF_{optics}, $MTF_{detector}$, and MTF_{system} calculated using the aforementioned methods.
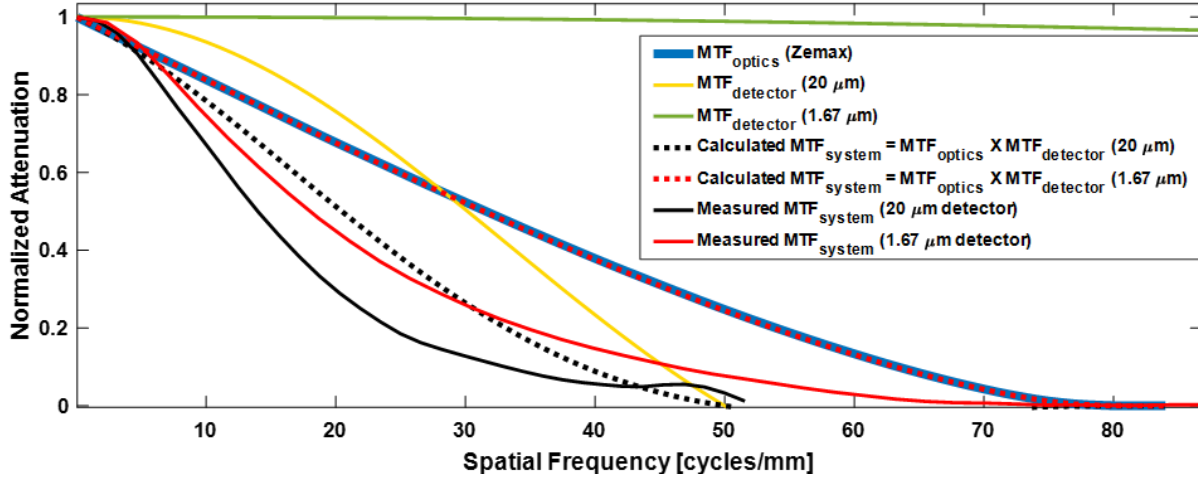

Figure 2: Comparison of modeled vs. measured MTF results for the 20 μm and 1.67 μm coaxial monitoring systems.

Multiple observations can be made about the optical system by comparing the curves in Figure 2. First, the measured MTF_{system} curves are below the modeled results, which is physically consistent. The calculated and measured MTF_{system} for the 20 μm detector cuts off at ≈ 50 cycle/mm, which corresponds to the measured curve. The 1.67 μm $MTF_{detector}$ is zero at approximately 598 cycle/mm (green curve), the 20 μm $MTF_{detector}$ cutoff is at ≈ 50 cycle/mm, and diffraction limited (Zemax) optics cutoff is ≈ 80 cycle/mm. Therefore the 20 μm detector limits the maximum resolvable spatial frequency for that detector, while the optics limit the maximum resolvable frequency for the 1.67 μm detector.

Since the calculated 1.67 μm $MTF_{detector}$ shows minimal attenuation, it essentially does not limit the optical system, so that calculated 1.67 μm $MTF_{system} ≈ MTF_{optics}$ (maximum physical resolution), and the measured 1.67 μm MTF_{system} describes the real optical performance of the system without detector size being a limitation. Since the measured MTF_{system} for the 1.67 μm detector is below this optimal curve, this indicates there are other contributing factors such as obscurations, aberrations, or misalignment that need to be investigated. Similarly, the measured MTF_{system} for the 20 μm detector is below the calculated curve. Overall, the measured resolution, defined as 10% of the MTF, is 33.1 cycle/mm for the 20 μm detector, and 44.2 cycle/mm for the 1.67 μm detector.

While MTFs provide a more appropriate and encompassing definition of spatial resolution as opposed to the iFoV, they do not fully describe the performance of an optical system for its intended purpose. For example, a 10 % MTF resolution of 44.18 cycle/mm does not mean that only $(44.18 \text{ cycle/mm})^{-1} = 22.6$ μm or larger objects can be measured. To more closely analyze the real effect of spatial resolution on co-axial MPM measurements, we can test objects that more nearly resemble melt pool images.

Aperture Measurements as Surrogate Melt Pool

Fox et al. measured melt pool track widths ex-situ made in a prototype version of the AMMT, and compared these measurements to various in-situ melt pool image widths calculated after thresholding and binarizing the images [13]. Ex-situ measured track widths were relatively consistent at 118 μm ± 4.3 μm (± one standard deviation). However, melt pool widths measured in-situ with the MPM camera depend on the grayscale level chosen. In Fox et al., this could vary by the diagonal distance between two pixels, or ± 28 μm. However, the additional effect of limited optical resolution could not be investigated solely with in-situ melt pool images. To imitate a melt pool image under controlled conditions and known geometry, precision apertures were placed above the fiber illuminator, and were subsequently imaged with the co-axial MPM and both detector sizes. The apertures ensure a uniform illumination, whereas real melt pool images are typically saturated at the hottest part of the melt pool, and have very high intensity gradients stemming from the high temperature gradients on the melt pool surface. The uniform illumination in the aperture is set below the saturation level of the imager, which ensures any signal attenuation or effect on size measurements from the images can be measured.

Apertures at 100 μm, 200 μm, 300 μm, and 500 μm were tested, with the manufacturer's stated diameter tolerance of ±5 % for each. The centroid of the aperture images is calculated, and X and Y profiles through the centroid are shown in Figure 3 for the 1.67 μm detector, and Figure 4 for the 20 μm detector. There is visible ghosting in the aperture images, which is an unfocused duplicate of the aperture slightly offset from the main image. This may be due to imperfect anti-reflective coating of one of the dozen or so mirrors, lenses, etc. in the optical path, and likely contributes to the sub-optimal MTF_{system} measured in the previous section. However, this ghosting cannot be easily discerned from a KE image or MTF, which demonstrates the value in using a variety of characterization tests.
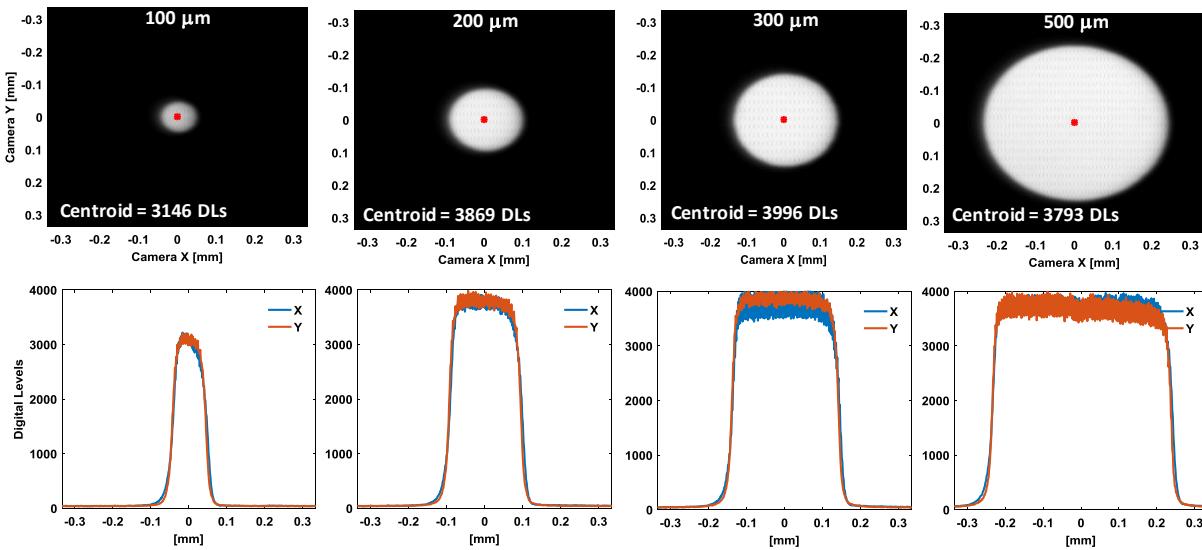

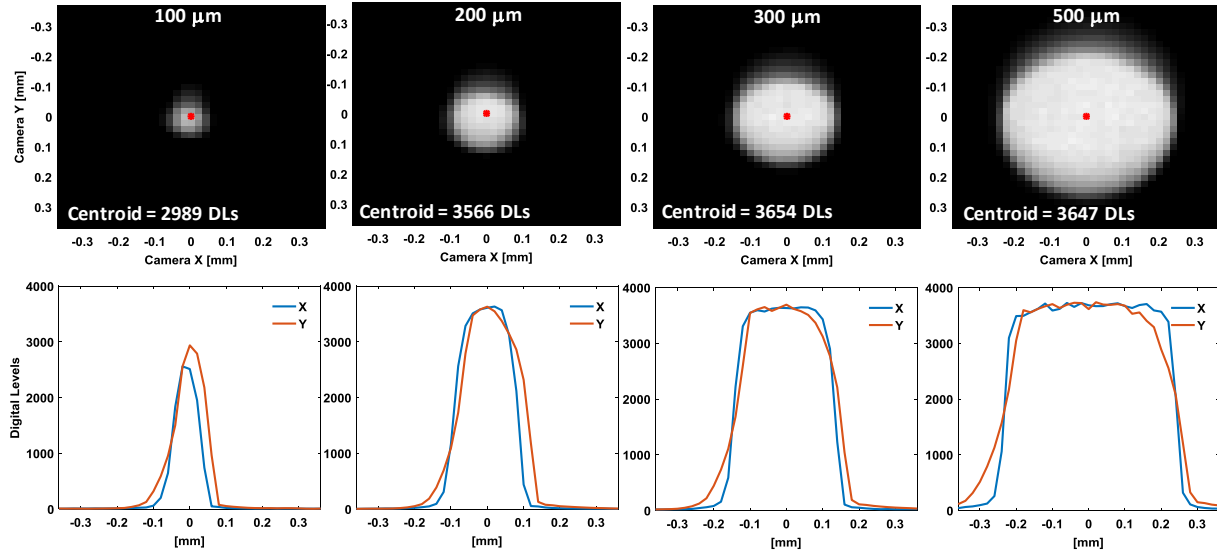Figure 3: Aperture measurement results for 1.67 μm detector.

Figure 4: Aperture measurement results for 20 μm detector.

One can see attenuation of maximum signal value for the 100 μm aperture for both the 20 μm and 1.67 μm detectors. A 100 μm aperture image may be considered ½ a cycle, or $w/2 = 100$ μm, which corresponds to $f \approx 5$ cycle per mm. At $f = 5$ cycle per mm, the $MTF_{detector} = 89$ % for the 20 μm detector and 92.3 % for the 1.67 μm detector. The measured attenuation is roughly 80 % for the 100 μm aperture measured by both detector sizes. It can be expected that smaller aperture sizes would result in further attenuation.

To further study the effect on a real melt pool measurement through image processing, geometric parameters from the melt pool images are calculated using the image processing toolbox in Matlab:

1.) Convert to 8-bit grayscale.
2.) Resize using sub-pixel interpolation (Matlab function 'imresize').
3.) Convert to binary images at three user-selected levels. The central binary image is used for further image processing and calculation.
4.) Calculate the centroid, major, and minor axes of the binarized melt pool image, and relative angle of these axes.
5.) Calculate the length and width of the melt pool along the major and minor axes, respectively.

It should be emphasized that the resizing function in step 2 interpolates between pixels, which results in sub-pixel resolution geometric measurements. Two example processed images of the 100 μm aperture are shown in Figure 5. The central, target gray level is set such that the 100 μm aperture image results in an accurate measure of the aperture width based on the detector iFoV as shown in Table 1. Two other gray levels contours are plotted at approximately ½ and 2x the central contour to show the shape of higher and lower levels. Width, length, and major axis angle are calculated from the image analysis for the four aperture sizes and two detectors.
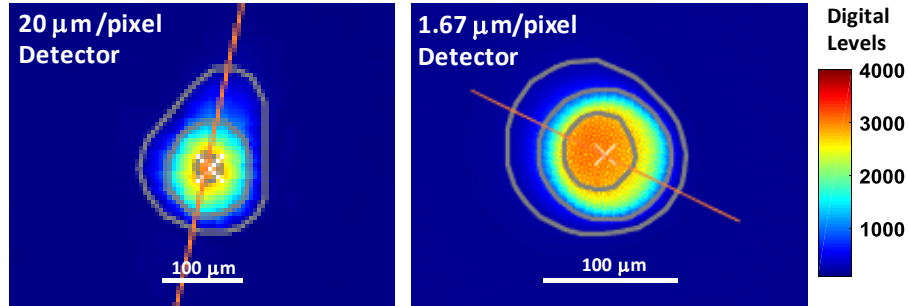
Figure 5: Example results from melt pool image analysis performed on back-illuminated 100 μm precision aperture. Note that image scales are not equal.

Table 1: Results from melt pool image analysis performed on precision apertures. Manufacturing tolerance on the apertures is ±5%.

Aperture	1.67 μm Pixel Camera			20 μm Pixel Camera		
	Width	Length	Angle	Width	Length	Angle
μm	μm	μm	degrees	μm	μm	degrees
100	100	115	78	100	105	-26
200	204	224	78	202	208	-20
300	300	322	75	294	301	-27
500	494	527	71	483	494	-33

The ghosting that was apparent in the raw aperture images is exemplified in in the lower grey level contour, creating an asymmetric shape, which causes the unequal length and width measurements. The angular difference is due to the fact the imagers are held in different orientations. In a real melt pool measurement, asymmetry in the optical performance may bias angle or MP direction calculation, particularly if lower grey levels, or lower temperature ranges in the melt pool, are the target measurement.

Analysis of Real Melt Pool Images

Due to exceedingly high temperature gradients in and around the melt pool, the limited dynamic range of an imaging sensor results in saturated pixels at the center of the melt pool image, and pixels at the detector noise floor surrounding it. The image gradient, or contrast, in between is also very high, which corresponds to high spatial frequencies on the MTF curve. In this way real melt pool images are similar to the previously analyzed aperture images, although the center of a melt pool very likely is not uniform intensity nor were the aperture images set to saturate the camera. While some effects of the real spatial resolution can be observed with the aperture images, analysis of real melt pool images elucidate further complexities.

In the following example, a single line on a bare nickel alloy 625 plate is scanned at 3.4 m/s and 400 W laser power. A second scan was performed at the same parameters, but with an approximately 100 μm layer of alloy 625 powder spread on top of the nickel alloy plate. Laser spot is approximately 100 μm full-width half max (FWHM). Frame rate of the co-axial MPM camera with 20 μm detector size is set to 30 000 frames per second, integration time t_{int} = 33 μs, and filtered to 850 nm ± 20 nm wavelengths. Figure 6 shows the raw melt pool images, process images, and processing results. Only one frame taken from the bare metal surface scan is presented since there was minimal variation between frames.

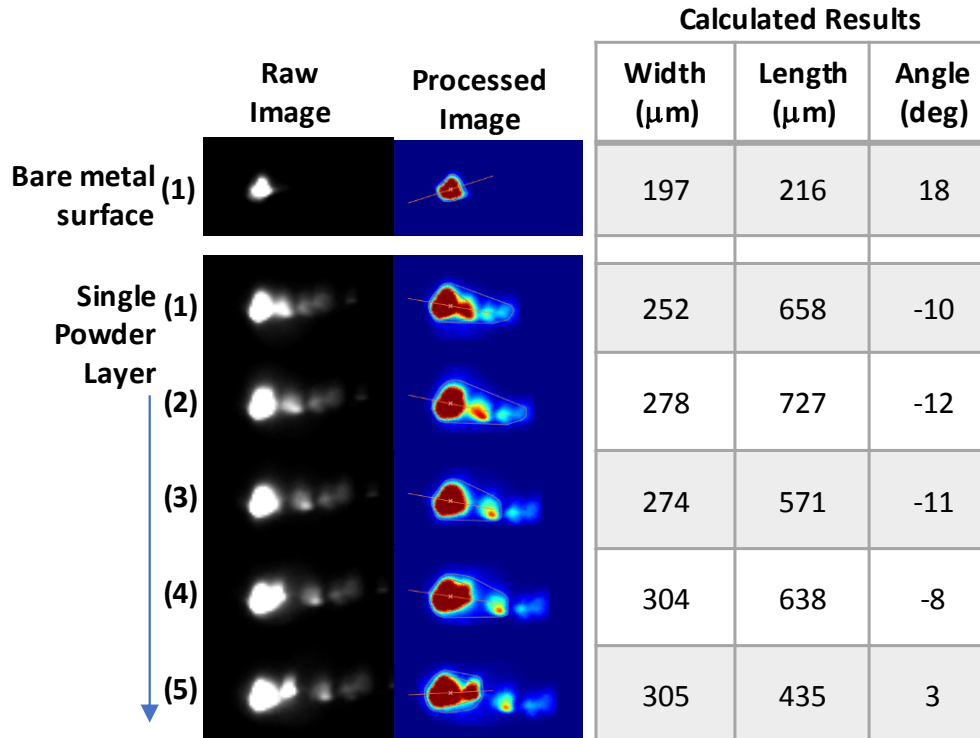|			Calculated Results		
	Raw Image	Processed Image	Width (μm)	Length (μm)	Angle (deg)
Bare metal surface (1)			197	216	18
Single Powder Layer (1)			252	658	-10
(2)			278	727	-12
(3)			274	571	-11
(4)			304	638	-8
(5)			305	435	3

Figure 6: Example MPM images and image processing results for the 20 μm imager. Top row is a single melt pool image when scanning bare metal, subsequent rows are high speed video frames while scanning a single-layer of powder.

The inclusion of powder adds complexity to the image analysis. Particle images still connected to main melt pool body will give erroneous size or angle measures, which is evident in Figure 6. Particles counting or frequency measurement may warrant additional image processing, as there is evidence to suggest spatter quantification may be correlated to AM track formation quality or process stability [21–23]. Since particles are at a lower temperature than the center of the MP; reducing integration time would effectively 'remove' particles from the MP images, but limit the measurement to only the highest apparent temperature regions of the MP, which may not be as sensitive the overall MP geometry changes.

Other potential factors limiting imager performance:

Blooming occurs when a region of pixels saturates due to excessive light flux, and the excess charge in the saturated pixels affects the signal output of adjacent pixels. Since it is nearly inevitable that melt pool images will have some portion saturated, blooming may have a significant effect on resultant apparent melt pool size measured via image processing. The light source used to create the aperture images in Figure 3 and Figure 4 was not bright enough. To evaluate the effect of blooming, a source intensity approaching that of a real melt pool is necessary[2]. Anti-blooming technologies exist; however, this changes the linear behavior of the detector (signal being proportional to incident light flux), which may introduce additional complexities in processing the images. In addition, detector linearity, or at least consistent flux to signal mapping, is essential for a radiant temperature calibration.

---

[2] Using Planck's law integrated over the 850 nm ± 20 nm waveband and evaluated at temperatures > 2500 K, and assuming the f-number of the system of 14.7 with opening aperture of 20 mm, this source flux would need to be on the order of 1 to 100 W/mm^2.

Motion blur is another resolution limiting factor, which is not widely discussed in co-axial MPM literature. The blur distance may be estimated as $v \cdot t_{int}$, with v being the linear motion velocity relative to the field of view frame of reference, and t_{int} being the camera integration time. Since the melt-pool image is stationary within the field of view for co-axial MPM systems, only fluctuations of the melt pool boundary or spatter particle motion may be of concern. Still, the exceedingly high radiant flux stemming from a laser-induced melt pool means relatively short t_{int} is required (e.g., $t_{int} = 33$ μs for the melt pool images in Figure 6). For melt pool geometry measurements, this may not be a concern, however, for spatter analysis it may.

Discussion and Future Work

Many AM process monitoring define 'resolution' as iFoV, whereas true image resolution should be defined in more comprehensive terms such as the MTF. Measuring MTF, and comparing against calculated design, can illuminate what are the limiting factors in the optical system. However, MTF in and of itself does not fully define the performance of a co-axial MPM system; the final image processing, which may achieve sub-pixel resolution, will determine the true precision. By modeling then measuring the MTF, non-optimized performance of the imaging system was discovered. Therefore, future work will entail sequential examination of each component in the optical system to determine the culprit.

Based on measurement of the apertures, and the sub-pixel averaging nature of the melt-pool image processing, both a 1.67 μm/pixel and 20 μm/pixel imagers performed approximately the same in calculating aperture diameter, despite one detector being over 10x in size and limiting the MTF. This is mostly due to the interpolating nature of the MP image processing. However, the aperture image analysis demonstrated how intensity values may still be attenuated, despite a less sensitive effect on geometric boundary measurement. This could have significant consequence if parameters such as melt pool intensity or average intensity levels, or calibrated temperature values, are the measurand output from image analysis. Beyond MTF, spatial resolution, and choice in image processing algorithm, further physical complexities in MPM of powder surfaces stem from the ejected particles or spatter. This can create errors in simple length, width, area, etc. parameterizations of the melt pool image, and may warrant additional image processing to quantify the particles, or remove their influence.

Ultimately, co-axial MPM system performance evaluation depends on what objective measurand is to be extracted from the images. A suite of spatial, temporal, and intensity characterization tests, and a thorough understanding of their consequence on the melt pool image analysis is necessary to enable this process monitoring tool to become the key technique for in-situ part qualification.

References

[1] A.D. Peralta, M. Enright, M. Megahed, J. Gong, M. Roybal, J. Craig, Towards rapid qualification of powder-bed laser additively manufactured parts, Integrating Mater. Manuf. Innov. (2016) 1–23. doi:10.1186/s40192-016-0052-5.
[2] J. Mazumder, Design for Metallic Additive Manufacturing Machine with Capability for "Certify as You Build," Procedia CIRP. 36 (2015) 187–192. doi:10.1016/j.procir.2015.01.009.
[3] Sigma Labs, In-Process Quality Assurance™ (IPQA®) Solutions | Sigma Labs, (2017). https://www.sigmalabsinc.com/node/5 (accessed July 27, 2017).
[4] S.K. Everton, M. Hirsch, P. Stravroulakis, R.K. Leach, A.T. C lare, Review of in-situ process monitoring and in-situ metrology for metal additive manufacturing, Mater. Des. (2016). doi:10.1016/j.matdes.2016.01.099.
[5] M. Grasso, B.M. Colosimo, Process defects and in situ monitoring methods in metal powder bed fusion: a review, Meas. Sci. Technol. 28 (2017) 044005. doi:10.1088/1361-6501/aa5c4f.

[6] E. Reutzel, A. Nassar, A survey of sensing and control systems for machine and process monitoring of directed-energy, metal-based additive manufacturing, Rapid Prototyp. J. 21 (2015) 159–167. doi:10.1108/RPJ-12-2014-0177.

[7] T.G. Spears, S.A. Gold, In-process sensing in selective laser melting (SLM) additive manufacturing, Integrating Mater. Manuf. Innov. 5 (2016). doi:10.1186/s40192-016-0045-4.

[8] G. Tapia, A. Elwany, A Review on Process Monitoring and Control in Metal-Based Additive Manufacturing, J. Manuf. Sci. Eng. 136 (2014) 060801–060801. doi:10.1115/1.4028540.

[9] T. Craeghs, S. Clijsters, J.-P. Kruth, F. Bechmann, M.-C. Ebert, Detection of process failures in Layerwise Laser Melting with optical process monitoring, Phys. Procedia. 39 (2012) 753–759.

[10] S. Clijsters, T. Craeghs, S. Buls, K. Kempen, J.-P. Kruth, In situ quality control of the selective laser melting process using a high-speed, real-time melt pool monitoring system, Int. J. Adv. Manuf. Technol. 75 (2014) 1089–1101. doi:10.1007/s00170-014-6214-8.

[11] Concept Laser, Sintavia uses QM Meltpool to Ensure Part Quality in Metal AM, Concept Laser. (2017). http://www.conceptlaserinc.com/sintavia-uses-qm-meltpool-ensure-part-quality-metal/ (accessed June 19, 2017).

[12] S. Berumen, F. Bechmann, S. Lindner, J.-P. Kruth, T. Craeghs, Quality control of laser- and powder bed-based Additive Manufacturing (AM) technologies, Phys. Procedia. 5, Part B (2010) 617–622. doi:10.1016/j.phpro.2010.08.089.

[13] J.C. Fox, B.M. Lane, H. Yeung, Measurement of process dynamics through coaxially aligned high speed near-infrared imaging in laser powder bed fusion additive manufacturing, in: Proc SPIE 10214 Thermosense Therm. Infrared Appl. XXXIX, Anaheim, CA, 2017: pp. 1021407-1021407–17. doi:10.1117/12.2263863.

[14] P. Lott, H. Schleifenbaum, W. Meiners, K. Wissenbach, C. Hinke, J. Bültmann, Design of an Optical System for the In-Situ Process Monitoring of Selective Laser Melting (SLM), Phys. Procedia. 12 (2011) 683–690. doi:10.1016/j.phpro.2011.03.085.

[15] B. Lane, S. Mekhontsev, S. Grantham, M. Vlasea, J. Whiting, H. Yeung, J. Fox, C. Zarobila, J. Neira, M. McGlauflin, L. Hanssen, S. Moylan, M.A. Donmez, J. Rice, Design, developments, and results from the nist additive manufacturing metrology testbed (ammt), in: Proc. 26th Annu. Int. Solid Free. Fabr. Symp., Austin, TX, 2016: pp. 1145–1160.

[16] K. Fliegel, Modeling and measurement of image sensor characteristics, RADIOENGINEERING-PRAGUE-. 13 (2004) 27–34.

[17] G.C. Holst, Holst's Practical Guide to Electro-optical Systems, JCD Publishing, Winter Park, FL, 2003.

[18] ISO 12233:2014, Photography - Electronic still-picture cameras - Resolution measurements, ISO, Geneva, Switzerland, n.d.

[19] M. Estribeau, P. Magnan, Fast MTF measurement of CMOS imagers using ISO 12333 slanted-edge methodology, in: Proc. SPIE, St. Etienne, France, 2003: pp. 243–252.

[20] B. Lane, E. Whitenton, Calibration and measurement procedures for a high magnification thermal camera, NIST Internal Report 8089, National Institute of Standards and Technology, Gaithersburg, MD, 2015.

[21] L.E. Criales, Y.M. Arısoy, B. Lane, S. Moylan, A. Donmez, T. Özel, Laser powder bed fusion of nickel alloy 625: Experimental investigations of effects of process parameters on melt pool size and shape with spatter analysis, Int. J. Mach. Tools Manuf. 121 (2017) 22–36. doi:10.1016/j.ijmachtools.2017.03.004.

[22] S.A. Khairallah, A.T. Anderson, A. Rubenchik, W.E. King, Laser powder-bed fusion additive manufacturing: Physics of complex melt flow and formation mechanisms of pores, spatter, and denudation zones, Acta Mater. 108 (2016) 36–45. doi:10.1016/j.actamat.2016.02.014.

[23] G. Repossini, V. Laguzza, M. Grasso, B.M. Colosimo, On the use of spatter signature for in-situ monitoring of Laser Powder Bed Fusion, Addit. Manuf. 16 (2017) 35–48. doi:10.1016/j.addma.2017.05.004.